Electrospinning and electrospraying of silicon oxycarbide-derived nanoporous carbon for supercapacitor electrodes

Aura Tolosa, Benjamin Krüner, Nicolas Jäckel, Mesut Aslan,
Cekdar Vakifahmetoglu, Volker Presser

Electrospinning and electrospraying of silicon oxycarbide-derived nanoporous carbon for supercapacitor electrodes

Aura Tolosa,[a,b] Benjamin Krüner,[a,b] Nicolas Jäckel,[a,b] Mesut Aslan,[a]

Cekdar Vakifahmetoglu,[c,*] Volker Presser[a,b,*]

[a]   INM - Leibniz Institute for New Materials, 66123 Saarbrücken, Germany.

[b]   Department of Materials Science and Engineering, Saarland University, 66123 Saarbrücken, Germany.

[c]   Department of Mechanical Engineering, Istanbul Kemerburgaz University, 34217 Istanbul, Turkey.

*   Corresponding authors. E-mail: cekdar.vakifahmetoglu@kemerburgaz.edu.tr; Tel: +90-2126040100 &
E-mail: volker.presser@leibniz-inm.de; Tel: +49-6819300177

Abstract

In this study, carbide-derived carbon fibers from silicon oxycarbide precursor were synthesized by electrospinning of a commercially available silicone resin without adding a carrier polymer for the electrospinning process. The electrospun fibers were pyrolyzed yielding SiOC. Modifying the synthesis procedure, we were able to obtain electrosprayed SiOC beads instead of fibers. After chlorine treatment, nanoporous carbon with a specific surface area of up to $2394 \ \mathrm{m^2 \cdot g^{-1}}$ was obtained ($3089 \ \mathrm{m^2 \cdot g^{-1}}$ BET). Electrochemical characterization of the SiOC-CDC either as free-standing fiber mat electrodes or polymer-bound bead films was performed in 1 M tetraethylammonium tetrafluoroborate in acetonitrile (TEA-BF$_4$ in ACN). The electrospun fibers presented a high gravimetric capacitance of $135 \ \mathrm{F \cdot g^{-1}}$ at $10 \ \mathrm{mV \cdot s^{-1}}$ and a very high power handling, maintaining 63 % of the capacitance at $100 \ \mathrm{A \cdot g^{-1}}$. Comparative data of SiOC-CDC beads and fibers show enhanced power handling for fiber mats only when the fiber network is intact, that is, a lowered performance was observed when using crushed mats that employ polymer binder.

Keywords:

Silicon oxycarbide; electrospinning; electrospraying; carbide-derived carbon; electrical double-layer capacitors

1. Introduction

Electric double-layer capacitors (EDLCs), also known as supercapacitors, are energy storage devices which present unique properties such as high rate handling and long cycle lifetime, but exhibit only a moderate energy density.[1, 2] In these systems, energy is stored by electrostatic adsorption of ions to the large surface area of nanoporous carbon electrodes.[3] Common supercapacitor electrodes consist of nanoporous carbon powder, possibly a conductive additive like carbon black, and a polymer binder.[4, 5] While necessary for mechanical stability, the polymer binder increases the electrical resistance and blocks access to a certain fraction of the carbon nanopores.[4] These limitations can be overcome by employing free-standing electrodes, like buckypaper or graphene sheets.[6, 7] Alternatively, continuous mats of highly interconnected ultrafine fibers (and in many cases even nanofibers) is possible via electrospinning. This way, free-standing and binder-free fiber mats can be obtained for direct use as supercapacitor electrodes.[8, 9] Continuous fibers in a non-woven mat form a percolated network which is expected to facilitate high power handling by exhibiting very high electrical conductivity (commonly factor 10 higher than for powder electrodes).[10]

For a high supercapacitor performance, careful optimization of the porosity is required to combine high power (transport-optimization) and high energy ratings (maximization of suitable micropores).[1] Among the large group of carbon nanomaterials, including graphene, carbon nanotubes, and carbon onions, commercial supercapacitors almost exclusively employ nanoporous activated carbon.[11] Particularly attractive tunable carbon nanomaterials belong to the family of carbide-derived carbons (CDCs).[12] For CDC synthesis, metal carbides,[13] carboxides,[14, 15] or carbonitrides[16] are chemically etched with halogens (most commonly gaseous Cl_2). This way, non-carbon atoms are effectively removed from the precursor as volatile metal chlorides. The resulting carbon structure depends on the temperature, structure of the precursor, and further synthesis conditions. Also, the resulting degree of carbon ordering, pore size distribution, and porosity characteristics can be finely tuned and optimized for different electrolyte systems.[17, 18] So far, the conformal nature and versatility of the CDC synthesis process has been adapted for the synthesis of powders,[19] thin films,[20] nanobeads,[21] and ultrafine fibers.[22, 23]

Although CDC had been widely synthetized from metal carbides powders such as TiC,[24] SiC,[25] B_4C,[26] VC,[27, 28] SiOC,[29] and NbC,[30] less attention was given to the synthesis of these materials with a specific morphology such as fiber shape. Metal carbide fibers can be produced in the form of non-woven mats by electrospinning of metal carbide molecular precursors at room temperature, which are later transformed into metal carbides by pyrolysis above 1200 °C.[31] By this approach, the only two systems explored have been TiC-CDC[32]' [22] and SiC-CDC.[23] The latter was produced using polycarbosilane (PCS) as precursor and did not presented uniform morphology.

Naturally, cost considerations are of high importance when employing advanced processing such as electrospinning. SiOC precursors, namely polysiloxanes and polysilsesquioxanes, are commercially available for relative low costs and have been positively evaluated as CDC precursor, but not yet for electrospun CDC fibers.[14] Therefore, in this study we focus on the production of SiOC-CDC fibers using a low cost commercially available polysilsesquioxane as precursor.

SiOC fibers had been produced by melt spinning of polysiloxanes[33] and by mechanical drawing of sol-gel systems,[34] yielding fiber diameters between 10-30 µm. In order to obtain thinner fibers electrospinning has been explored and for this method, adjusting the rheological parameters of the solution is of critical importance.[35] To achieve beneficial spinnability, commonly a carrier polymer is added to the spinning dope. So far, all reported electrospun SiOC fibers from preceramic polymers have made use of carrier polymer.[36] By introducing a polymer which can be easily electrospun, uniform, and smooth fibers can be obtained. The electrospinning of PCS and tetraethyl orthosilicate (TEOS) has been accomplished by adding polyvinyl butyral (PVB) or polystyrene (PS), obtaining fibers in the range of 0.5-1.5 µm.[37] Guo et al.[38] have reported the production of electrospun SiOC fibers from silicone resins, using polyvinylpyrrolidone (PVP) as a carrier polymer. The as-spun fibers, containing 75 mass% silicone resin and 25 mass% PVP, showed fiber diameters between 1.0-2.7 µm. In order to transform the as-spun fibers into ceramic fibers, a latent catalyst was added helping to maintain the fiber shape during the thermic process for transformation to SiOC. However, adding a carrier polymer, such as PVP or PAN, severely increases the process cost and produces undesired products by the decomposition of the carrier polymer.

Our work presents for the first time an approach to obtain continuous SiOC electrospun fibers without adding any carrier polymer. We also take advantage of the versatile transition from fiber-synthesis via electrospinning to obtain beaded materials via electrospraying by adjusting the process parameters. The obtained fibers and beads were then transformed into SiOC-CDC and evaluated as electrodes for supercapacitors. To the best of our knowledge, this study is also the first to present CDC beads from electrospray synthesis. The performance of the fiber mat was compared to rolled electrodes containing polymer binder, one containing milled SiOC-CDC fibers and another containing SiOC-CDC beads. This enables us to gain important insights in the electrochemical performance and power handling ability when comparing, for the same material, different shape (beads vs. fibers) and electrode design (interconnected fibers and binder-free vs. broken fibers with binder).

2. Experimental

2.1 Materials

Ethanol (≥99.8 %) and N,N-dimethylformamide (anhydrous, 99.8 %) were purchased from Sigma Aldrich. Commercial silicone resin, namely H44 (polymethylphenyl-silsesquioxane) was purchased from Wacker Chemie. Moisture sensitive catalysts zirconium(IV)acetylacetonate (ZrAcAc), and zinc acetylacetonate hydrate powder (ZnAcAc) were purchased from Sigma Aldrich and stored in moisture free N_2 atmosphere in a glove box (H_2O, $O_2 < 0.1$ ppm). All chemicals were used as-received.

2.2 Synthesis of SiOC fibers and beads

Before preparing the spinning dope, H44 was partially crosslinked by heating as-received powder to 200 °C in air. The pre-crosslinked resin H44 was cooled to room temperature and ground into a powder using an agate mortar and pestle.

The spinning dopes were prepared at ambient conditions, containing 56 mass% of silicone resin and 6 mass% of ZnAcAc in ethanol and/or DMF. All solutions were stirred for 24 h. Electrospinning and electrospraying were carried on a MECC Co. NF-103V nanofiber system. The spinning dope was pumped at 1 mL·h^{-1} through a spinneret (inner diameter: 510 μm), which was inductively charged at 28 kV. The fibers and beads were collected on a stationary grounded target at a distance of 21 cm from the spinneret. The collected material was then heated at 100 °C for 24 h to stabilize the fiber/bead shape. Complete crosslinking of the silicone resin was accomplished by heat treatment at 200 °C for 2 h.

The pyrolysis of the crosslinked silicone resin was achieved by heating the material at 5 °C·min^{-1} to 1200 °C for 2 h, under argon in a graphite heater (Thermal Technologies, Model: 1100). After heat treatment SiOC nonwoven mat and beads were cooled at a rate of 20 °C·min^{-1} to room temperature.

2.3 Chlorine gas treatment

Carbide-to-carbon conversion by chlorine gas treatment (CDC process) was carried on a quartz tube furnace HTRH, Gero, constantly purged with argon (50 cm^3·min^{-1}). The SiOC produced was heated at a rate of 15 °C·min^{-1} to 1200 °C, and treated with chlorine gas for 3 h (10 cm^3·min^{-1}). During cooling, a post annealing process with hydrogen gas (10 cm^3·min^{-1}) was applied at 600 °C for 3 h in order to remove residual chlorine and chloride species present in the sample. The mass of the sample was measured before and after the chlorine treatment.

2.4 Materials characterization

The molar mass of the silicone resin was determined by high performance liquid chromatography-gel permeation chromatography (HPCL-GPC) using automatic injection (Agilent 1260 Infinity). The calibration was carried out with PDMS-standards in toluene. The melting of the silicone resin and the decomposition of the catalysts were determined by differential scanning calorimetry (DSC). All measurements were carried in air at $5\,°C·min^{-1}$. Thermogravimetric analysis (TGA) of the metal acetonates was carried out in O_2 with a SDT Q26 system, TA instruments, using a heating rate of $10\,°C·min^{-1}$.

The morphology of the sprayed or spun material was examined by a JEOL JSM 7500F field emission scanning electron microscope (FE-SEM). All samples were fixed on steel sample holders with sticky carbon tape. The as-spun and crosslinked fibers were sputter coated prior to the imaging with a thin layer of platinum in a JEOL Autofine Coater. ImageJ software[39] was used to process the SEM images and diameters of at least 150 individual fibers or beads were measured. High resolution transmission electron microscope images (TEM) were carried in a JEOL JEM-2100F system at 200 kV in vacuum. TEM samples were prepared by dispersing and sonicating the fibers in ethanol and drop casting them on a copper grid with a lacey carbon film. The composition of the fibers was measured by energy dispersive X-ray spectroscopy (EDX) using a X-Max-150 detector from Oxford Instruments attached to the SEM chamber. Using an accelerating voltage of 5 kV and an emission current of 10 µA, the spectra of 10 different fibers or beads were measured and the average values were calculated.

X-ray diffractograms were collected with a Bruker D8 Discover diffractometer using Cu-K$_\alpha$ radiation (0.154 nm) with a step size of 0.02 ° and a measurement time of 1 s per step. The system was calibrated with an alumina single crystal.

Infrared vibrational spectroscopy was performed with a diamond total attenuated reflectance crystal (ATR) using a Bruker Tensor 27 FTIR system (Fourier transform infrared spectroscopy). Raman spectra were recorded with a Renishaw InVia Raman system using a laser with a 532 nm excitation wavelength and 0.5 mW power on the sample with a spectral resolution of ca. 1.2 cm^{-1}, using a 50x objective (numeric aperture: 0.9). Peak analysis and peak fitting were performed assuming four Voigt peak fitting between 500 and 2000 cm^{-1}.

Nitrogen gas sorption measurements at -196 °C were carried out with an Autosorb iQ system (Quantachrome). The samples were outgassed at 300 °C for 10 h under vacuum conditions (about 10^2 Pa) to remove adsorbed water and other volatile surface functionalities. The relative pressure range was sampled from $5·10^{-7}$ to 1.0 in 68 steps. The specific surface area (SSA) was calculated with the ASiQwin software using the Brunauer-Emmett-Teller (BET) equation[40] in the linear relative pressure range 0.05-0.2. We also calculated the SSA and pore size distribution (PSD) via quenched-

solid density functional theory (QSDFT)[41] with assuming slit-shaped pores and pore size between 0.56 and 37.5 nm. Values for the total pore volume correspond to $p/p_0 = 0.95$. CO_2 gas sorption measurements were carried out at 0 °C in the relative pressure range from $1 \cdot 10^{-4}$ to $1 \cdot 10^{-2}$ in 40 steps. SSA and PSD values were calculated for pore sizes between 0.3 and 1.0 nm with the ASiQwin software using nonlocal density functional theory (NLDFT) for CO_2 sorption.[42, 43]

2.5 Electrochemical characterization

For the electrochemical characterization, free-standing fiber mats and film electrodes containing polymer binder were used. The polymer binder containing electrodes were prepared using SiOC-CDC beads or SiOC-CDC ground fibers. SiOC-CDC fibers and beads were ground with an agate mortar in ethanol until obtaining a homogeneous slurry, to which 13 mass% polytetrafluoroethylene (PTFE, 60 mass% solution in water, Sigma Aldrich) was added. The obtained paste was rolled until 140±20 µm thick electrodes were obtained (MTI HR01 rolling machine, MTI). Prior to use, the electrodes were dried at 2 kPa, 120 °C for 48 h.

The performance of the electrodes was evaluated using a half- and full-cell setup in 1 M tetraethylammonium tetrafluoroborate (TEA-BF_4) in electrochemical grade acetonitrile (ACN) from BASF. The electrodes were tested in custom-built polyether ether ketone (PEEK) cells with spring loaded titanium pistons. Half-cell tests were performed with an oversized counter electrode (YP-50, Kuraray Chemicals). The working electrode discs with 8 mm diameter were punched out of the PTFE-bound electrodes and the free-standing fiber mats. The electrode pair was separated by a glass-fiber separator (GF/D from Whatmann) and placed between 12 mm diameter carbon-coated aluminum current collectors (Zflo 2653, Exopack technologies, USA). YP-50F with 5 mass% PTFE was used as the reference. The assembled cells were dried at 2 kPa, 120 °C for 24 h. After cooling down the cells were placed in an inert gas glove box (MBraun Labmaster 130, O_2 and H_2O <1 ppm), and filled with 1 M TEA-BF_4 in ACN.

Electrochemical measurements were carried out with a potentiostat/galvanostat (VSP300 from Bio-Logic), by cyclic voltammetry (CV) and galvanostatic cyclic potential limitation (GCPL). CVs were recorded at 10 mV·s^{-1} scan rate in the potential range from 0 V to +2.7 V for full-cell and from -1 V to +1 V in half-cell versus carbon. Galvanostatic cycling was carried from -1 V to +1 V in a three-electrode setup (i.e., half-cell) at 2 A·g^{-1} with a holding time of 10 min. The capacitance was calculated by use of *Eq. (1)*, with C_{sp} specific capacitance, t_0 starting time, t_{end} end time of discharge and, U cell voltage. The specific capacitance corresponds to the capacitance related only to the active mass material (mass of polymer binder was not considered). The parameter X corresponds to 1 for a half-cell and to 4 for a full-cell (i.e., two-electrode system).[2]

Eq. (1) $\qquad C_{sp} = \frac{X}{m} \cdot \frac{\left(\int_{t_0}^{t_{end}} I dt\right)}{U}$

Performance stability tests were carried out over 10,000 cycles of voltage cycling at 2.7 V at 50 mV·s^{-1}. Electrical impedance spectra were recorded in symmetrical full cells for 100 kHz to 100 mHz at 0 V with 10 points per decade and averaged over 5 measurements.

3. Results and Discussion

3.1 Electrospinning of polymethylphenyl-silsesquioxane fibers

In order to electrospin H44, we first had to establish optimized processing parameters, such as a suitable solvent (ethanol) and polymer concentration (60 mass%; see *ESI*, **Figure S1**). After the electrospinning process, the fibers are transformed into an infusible thermoset, which for silicone resin typically occurs by heating above 200 °C. However, at 42 °C the as-received H44 melts (**Table 1**) and the fiber integrity is lost before complete crosslinking is achieved at 200 °C.

Reduced softening or promoting of crosslinking at lower temperatures can be achieved by adding latent catalysts such as metal acetylacetonates.[38, 44] According to Smith,[45] the decomposition products of metal acetylacetonates may be the active species which activate the crosslinking of the polymer at lower temperatures. Each metal acetylacetonate will decompose at a different temperature; however, the decomposition occurs typically above the melting point of the silicone resin, for example for ZnAcAc and ZrAcAc (see *ESI*, **Figure S2**). When adding 0.05 parts of latent catalyst per part of silicone resin, fiber melting is observed before the activation of the catalyst (see *ESI*, **Figure S3**). Thus, direct pyrolysis after electrospinning of H44 fibers is not possible and a modified approach needs to be applied, the most attractive one being pre-crosslinking.

3.1.1 Pre-crosslinking

The melting behavior of the polymers can be modified when the molecular weight of the polymer is increased by partial crosslinking. In such cases, the higher entanglement and interaction between the chains will restrict translational movements of the chains, and more energy is required for the melting of the polymer.[46, 47] We explored pre-crosslinking of the H44 precursor prior to electrospinning in order to ensure the integrity of the fibers during curing process. After electrospinning, stabilization of the fiber shape can be accomplished at a temperature below the melting point of the polymer which is still sufficiently high to promote the catalytic activity of the metal acetylacetonate, such as ZnAcAc. H44 was pre-crosslinked at 200 °C for 2 h (H44-22) and 6 h (H44-26) and the change on molecular weight and the melting point compared to the as-received state of H44 is given in **Table 1**.

An increase of 60 % in the average molecular weight lead to an increase of 16 °C in the melting point in the case of H44-26. Further increase in the molecular weight comes at the cost of decrease in the solubility of the precursor polymer. In order to compare the effect of pre-crosslinking on the microstructural evolution, spinning dopes were prepared containing 60 mass% of silicone resin in ethanol using H44 and H44-26 resin. A total of 0.1 parts of latent catalyst (ZnAcAc) per part of silicone resin was added, for a solution with a concentration of 56 mass% silicone resin and 6 mass% ZnAcAc. The melting behavior of the spun fibers was confirmed by SEM as shown in **Figure 1** and by DSC of dried spinning dopes, in both cases after stirring the spinning dope for 24 h (see *ESI*, **Figure S4**). It can be observed that the catalyst concentration and the pre-crosslinking have an influence in the melting point of the fibers. For as-received H44, by adding 0.1 parts of catalyst per part of silicone resin (**Figure 1a**), the fibers partially melted at 80 °C, while fibers had completely melted when adding just 0.05 parts of catalyst (see *ESI*, **Figure S3d**). When adding 0.1 parts of catalyst to the as-received and pre-crosslinked resin (**Figure 1**), the pre-crosslinking increased the melting point of the system. The H44-26 fibers maintained the shape by heating to 100 °C with a melting point of the system of about 120 °C, which is ca. 30 °C higher than for the H44 fibers (see *ESI*, **Figure S4**). The thermal decomposition of ZnAcAc occurs in the range of 100-120 °C (see *ESI*, **Figure S4**), meaning that crosslinking reactions can be promoted at ca. 100 °C and the fiber shape can be maintained in consequence.

3.1.2 Optimization of fiber diameter

Aiming to produce fibers as thin as possible, two parameters were modified separately: (i) polymer concentration, and (ii) dielectric constant of the solvent. While each parameter can promote the formation of thinner fibers, an increase in the surface tension or a decrease in the viscosity promotes the formation of beads.

First, the polymer concentration was decreased relative to the solvent from 60 to 50 and 40 mass% (see *ESI*, **Figure S5**). By doing so, symmetrical instabilities were promoted due to the low viscosity of the system and high surface tension, leading to beaded fibers and beads formation. The bead's collapsed skin was related to the rapid loss of the solvent.[48] By keeping the polymer concentration constant at 60 mass% relative to the solvent, the dielectric constant was then modified by adding a solvent with a higher dielectric constant than ethanol (EtOH). Dimethylformamide (DMF) presents a higher dielectric constant but yields also higher surface tension;[49] therefore, spinning dopes were prepared from the blends of DMF/EtOH. The obtained morphologies are shown in **Figure 2**.

Different DMF/EtOH mass ratios between 0 to 1 were evaluated. When using more than 0.1 of DMF, the surface tension of the system increased by such a large amount that beaded fibers were formed. When using 1/0 and 0.5/0.5 ratios of DMF/EtOH, electrospraying occurred yielding beads with an

average size of 3.3±0.8 µm and 2.5±0.6 µm were obtained, respectively (**Figure 2c**). The as-spun fibers by using only ethanol presented a fiber diameter of 5.0±2.5 µm (**Figure 2f**). By using 0.1/0.9 of DMF/EtOH, the fiber diameter decreased to 2.2±1.4 µm (**Figure 2d**) which was the smallest diameter we were able to obtain. In addition to the change in fiber diameter, also the fiber morphology was modified. When using just ethanol, the observed fiber morphology was mostly ribbon-like, and increasing the DMF content caused an increase in the formation of cylindrical cross sectioned fibers. The presence of ribbons is related to the interaction phenomena of mechanical forces and the solvent evaporation at scales above 1 µm.[48]

3.2 From polymethylphenyl-silsesquioxane to SiOC and SiOC-CDC

After optimizing the crosslinking of the system and fiber morphology, two different systems were chosen: (1) free-standing fiber mats produced using 0.1/0.9 of DMF/EtOH and (2) beads produced using 1/0 of DMF/EtOH. The mats and beads were further treated at 200 °C for 2 h to ensure complete crosslinking prior to the pyrolysis. They were later transformed to SiOC by pyrolysis under Ar at 1200 °C for 2 h. The process resulted in a cumulative mass loss of 29 %, and led to SiOC, where an excess of carbon relative to stoichiometric SiOC precipitates (called as "free carbon"; stoichiometric SiOC:$SiO_{2(1-x)}C_x$, see **Table 2**).[50]

The fibers and beads were then treated with chlorine gas to remove non-carbon atoms from the material.[12] During thermal chlorine treatment of SiOC, the SiC and SiO_2 domains react in the presence of carbon according to *Eq. (2)-(3)*, removing the silicon and oxygen as volatile species, and leading to a highly porous carbon.[32]

Eq. (2) $\quad SiC + 2Cl_2 \rightarrow SiCl_4 + C$

Eq. (3) $\quad SiO_2 + 2C + 2Cl_2 \rightarrow SiCl_4 + 2CO$
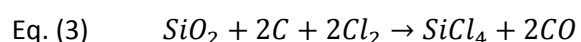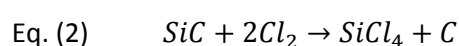
The chlorine treatment for the fibers and beads yielded a mass loss of 82-85 mass%, leaving behind almost pure carbon. As seen from **Table 2**, the material contained ca. 2 at% of oxygen, but no other elements were detected. The beads showed small amounts of residual silicon (0.2 at%) and chlorine (2 at%) as a result of the much larger bead diameter, indicating slightly incomplete transformation to CDC.

With FTIR, we tracked the solvent evaporation, and hydrolysis and condensation reactions during crosslinking (**Figure 3a**). A broad peak centered at 3330 cm^{-1} related to terminal O-H bonds present in ethanol and in the silicone resin disappeared in the crosslinked fibers.[51] The Si-O stretching vibration in the Si-O-Si ladder structure appeared between 1041-1026 cm^{-1},[52] overlapping with a peak present at 1084 cm^{-1} related to C-N bridging vibrations in DMF, and a peak at 1130 cm^{-1} related

to phenolic groups present in the silicone resin.[51] Peaks observed at 1268, 2970, and 2927 cm^{-1} are related to the C-H vibration modes from the methyl groups.[51] Absorbance of the bridging bond Si-C in the SI-CH$_3$ was observed at 734 cm^{-1}.[52] In the pyrolyzed sample, the only visible bands correspond   to Si-O-Si (980 cm^{-1}) and Si-C (715 cm^{-1}).[52] This confirms the formation of SiOC ceramic material. Both signals disappear after chlorine gas treatment, related to the removal of Si atoms as SiCl$_4$ and the emergence of highly pure carbon, with hydroxyl groups bonded to the carbon, related to the broad peak at 3330 cm^{-1}. However, a broad and small peak can be seen at 980 cm^{-1} in the spectra of SiOC-CDC beads, confirming the incomplete transformation to CDC.

Raman spectroscopy allows to characterize the degree of ordering of the free carbon phase within in the SiOC matrix and the structure of SiOC-CDC. The measured spectra (**Figure 3b**) showed two peaks characteristic for incompletely graphitized carbons, namely the D-mode between 1335 cm^{-1} and 1346 cm^{-1} and the G-mode between 1599 cm^{-1} and 1607 cm^{-1}. In addition, we see combination modes and overtones between 2500 cm^{-1} and 3000 cm^{-1}. D- and G-mode relate both to sp^2-hybridized carbon; the G-mode is related to the bond stretching of pairs of sp^2-hybridized carbon atoms in rings and chains,[53] and the D-mode is due to the activation of the breathing modes of six carbon atoms rings when a defect is present.[54] The shift of the G peak from 1581 cm^{-1} for pure graphite to 1600 cm^{-1} is related to the coexistence of amorphous carbon (1550 cm^{-1}), nanocrystalline graphite, and sp^2-hybridized carbon chains.[54] For the characterization of the D- and G-mode, a four peak Voigt fitting was applied (see *ESI*, **Figure S6**) to deconvolute the peaks related to amorphous carbon and trans-polyacetylene (TPA, between 1200 cm^{-1} and 1260 cm^{-1}), in addition to the dominant D- and G-mode. The combined data of the integral I_D/I_G ratio and full-width at half-maximum (FWHM) for SiOC and SiOC-CDC (**Table 2**) give information about the degree of carbon ordering. The free carbon in SiOC fibers and beads presents an in-plane correlation length L_a (often seen as domain or crystalline size) of 3.4 nm and 3.6 nm respectively, calculated by the Tuinstra-Koenig relation.[55, 56] After chlorine gas treatment, a new carbon phase is formed. Considering the high chlorine gas treatment temperature (1200 °C), graphitization is promoted for the formed carbon phase and the already existing phase, meaning a lower presence of amorphous carbon but a smaller average in correlation length of the nanocrystalline carbon (L_a ca. 3.0 nm and 2.8 nm for fibers and beads respectively). This observation aligns well with the measured FWHM decrease for both modes.

X-ray diffraction (XRD) and TEM analysis allow to follow the structural transition from the amorphous as-spun fibers after thermal stabilization at 200 °C to the SiOC ceramic material with a highly disordered structure after pyrolysis to partially graphitic carbon (SiOC-CDC) after chlorine gas treatment (**Figure 4**). Additionally, SEM allows us to observe the changes in the fiber morphology caused by the process. After the treatment at 200 °C of the H44-26, a partial melting was observed

between the points of contact of the fibers (**Figure 4b)**, but the open percolated network and the characteristic fiber morphology was maintained. The open percolated morphology was also maintained after pyrolysis (**Figure 4c**) and thermal chlorine gas treatment (**Figure 4d**).

XRD pattern of the polymer H44-26 (**Figure 4a**) allow to characterize the ladder structure of the polymer.[57] The peak at 8.4° 2θ indicates a plane-to-plane distance corresponding a chain-to-chain distance of d_1 = 1.05 nm. The peak at 19.7° 2θ represents a thickness of the molecular chains of d_2 = 0.45 nm.[57] The XRD pattern of SiOC is typical for an amorphous material in agreement with TEM (**Figure 4c,e**). For SiOC, no distinguishable peaks can be identified related to α-cristobalite or β-SiC due to highly disordered character of the material at such pyrolysis temperatures. After chlorine treatment, the decrease in density resulting from etching non-carbon species is evidenced by TEM micrographs (**Figure 4d,f**). The XRD pattern for SiOC-CDC is characteristic of amorphous/disordered carbon with a distinguishable peak around 44° 2θ related to the (10)-reflection from the graphene layer plane.[58] Applying the Scherrer equation,[59] the average in-plane coherence length is estimated to be around 3-4 nm for the SiOC-CDC fibers and beads, which is similar to the value obtained from the Raman spectra when applying the Tuinstra-Koening equation.[56] The lack of a distinct (002)-graphite reflection at around 26° 2θ is related to a lack of stacking of the graphite layers or a high disorder of the stacking.[58]

Furthermore, SiOC and SiOC-CDC samples were characterized by gas sorption analysis with N_2 and CO_2 for the determination of the pore structure (**Figure 5**). According to the N_2 sorption isotherms (**Figure 5a**), SiOC presents a Type II isotherm characteristic of nonporous solids.[60] After chlorine treatment, the material corresponds to a highly microporous material, characterized by a Type I(b) isotherm, presenting a broader range of micropores and narrow mesopores.[60, 61] The pore size distribution of the material was characterized by N_2 gas sorption for pores of 0.9-35 nm and by CO_2 gas sorption for pores <0.9 nm. The cumulative pore volume increased from around 0.01 $cm^3 \cdot g^{-1}$ for SiOC to 1.78 $cm^3 \cdot g^{-1}$ and 1.41 $cm^3 \cdot g^{-1}$ after chlorine gas treatment, for the fiber and beads respectively. The SiOC-CDC fibers present a very high BET specific surface area of 3089 $m^2 \cdot g^{-1}$ (QSDFT: 2394 $m^2 \cdot g^{-1}$), and the SiOC-CDC beads present a BET specific area of 2227 $m^2 \cdot g^{-1}$ (QSDFT: 1679 $m^2 \cdot g^{-1}$). Both SiOC-CDC presented similar average pore size (ca. 1.6 nm), but beads exhibit a lower cumulative pore volume and specific surface area considering the incomplete CDC transformation. The BET surface area of SiOC-CDC fibers belongs to the highest values reported for CDCs so far,[14, 29, 62] currently only surpassed slightly by SiC-CDC of Rose et al.[23] (3116 $m^2 \cdot g^{-1}$).

3.3 Electrochemical performance of SiOC-CDC electrodes

The electrochemical performance of the SiOC-CDC electrodes was evaluated by cyclic voltammetry and galvanostatic cycling. By comparing different particle morphologies, we aim to establish a better

understanding of the advantages of a continuous material network versus a non-continuous material for electrodes. We provide for the first time comparative data for SiOC-CDC fibers used as binder-free, free-standing electrode mats (**Figure 4d,** *inset*) or as PTFE-bound films using either SiOC-CDC beads (**Figure 4f,** *inset*) or crushed fibers. The reported specific capacitance values are based only on the active material for a fair comparison between binder-free electrodes and PTFE-bound films.

Cyclic voltammograms of the half-cell setup recorded at 10 mV·s^{-1} in 1 M TEA-BF$_4$ in ACN are shown in **Figure 6a** and galvanostatic charge-discharge capacitance values vs. electrode potential (vs. carbon) are plotted in **Figure 6b**. Negative or positive polarization led to a constant increase of the capacitance with electrode potential. This effect is well-known and related to the increase in density of states in the nanocrystalline graphite.[63] The increase corresponds to 175-200% of the value at 0 V and was observed in all electrodes. A higher capacitance was observed in half-cell setup for positive potentials related to difference in size of the anion and cation, leading to a higher confinement for BF$_4^-$ than for TEA$^+$.[64] Using to Eq. (1), a specific capacitance of 135F·g^{-1} or 110 F·g^{-1} at 1 V vs. carbon was obtained for free-standing fiber mat and PTFE-bound beads, respectively. Using GCPL (**Figure 6b**), the fibers electrodes present a specific capacitance at +1 V of 120 F·g^{-1} (binder-free) and 114 F·g^{-1} (PTFE-bound) compared to 112 F·g^{-1} for SiOC-CDC beads. All these values fall within a ±10 % range of statistical variation. Even though normalized to the mass of carbon (i.e., correcting for the binder-content), the PTFE-bound fiber electrode still shows a lower capacitance value. This can be explained by pore blocking due to the presence of binder compared to the binder-free free-standing fiber mat electrodes.[5]

While the near-equilibrium performance (i.e., at low rate) of binder-free and binder-bound electrodes are very similar, the behavior is very different for the power handling ability. We already see the much faster response of the binder-free fiber electrode in the CV shown in **Figure 6a** with the steep increase and weakly pronounced resistive knee at the vortex potentials. Furthermore, the impedance of the free-standing fiber mat is different from the PTFE-bound electrodes (**Figure 6c**). The electrical serial resistance (ESR) of the fiber mat is 0.62 Ω·cm^2, which is smaller than for the PTFE-bound electrodes (0.82 Ω·cm^2, **Table 3**). The difference in the ESR value is related to the lower internal resistance of the continuous fibers and a higher particle-particle contact resistance for the PTFE-bound electrodes. The electrical distribution resistance (EDR) is 0.09 Ω·cm^2 for the free standing fibers. This behavior changes for the PTFE-bound electrode, where the EDR is larger (0.17 and 0.15 Ω·cm^2, for fibers and beads, respectively) because of the higher particle packing and the larger diffusion length of ions. Regarding very low frequencies, the constant phase element (CPE) of the free standing fiber mat is more pronounced, having an exponent of 0.83 and we explain this by the very inhomogeneous thickness of the fiber mat in comparison to the homogenously compacted and

rolled particles in the PTFE-bound electrode.[65] The exponent of the CPE for the polymer-bound electrodes is very close to 1 related to an ideal capacitive behavior (**Table 3**).

When evaluating the rate capability for full-cell by GCPL between 0.1 A·g^{-1} to 100 A·g^{-1} a drastic difference between the electrodes is observed (**Figure 6e**). At 10 A·g^{-1}, the free-standing fiber mat electrode retains 86 % of the capacitance at 0.1 A·g^{-1}, while the PTFE-containing electrodes retain 80 % and 73 % of the capacitance. At 100 A·g^{-1}, the PTFE-containing electrodes had completely lost the capacitance, while the fiber mat was still able to maintain 63 % of the initial.

When comparing SiOC-CDC fibers with and without binder, we see although using the same carbon with the same porosity, pore structure, and particle size, an enhanced power handling can only be capitalized in the case of a continuous carbon fiber network. When comparing the two binder-containing electrode systems, we found a lower rate handling ability for the fibers compared to the SiOC-CDC beads (**Figure 6e**). This can be explained by the higher number of micropores found in SiOC-CDC fibers (i.e., inaccessible pores for ions), and also the better compaction of the beads compared to ground fibers. These considerations can also be seen for full-cell tests at 10 mV·s^{-1} (**Figure 6d**), where a specific capacitance of 130, 116, and 117 F·g^{-1} (maximum value at 2.7 V: 188, 176, and 164 F·g^{-1}) was obtained for the fiber mat, PTFE-bound beads, and PTFE-bound fibers, respectively. It can be seen that fibers and beads electrodes present similar capacitance values, showing that an enhanced porosity does not necessarily translate to an increased capacitance in organic media. Korenblit et al., for example, obtained larger capacitance values (125-150 F·g^{-1}) for SiC-CDC powder electrodes, which present a lower SSA value than the material synthesized in this work.[62]

In the full-cell, all electrodes showed a good performance stability over 10,000 of charge/discharge cycles at 50 mV·s^{-1} at 2.7 V (**Figure 6f**). Within the scatter of the method, we cannot see a statistically significant difference between the electrode materials' cycling stability. All samples showed after 10,000 cycles a decrease of just ca. 11 %. Yet, a comparison with the literature is difficult because the stability of SiOC-CDC powder electrodes in the same electrolyte had only been measured by voltage cycling at 2 V with a value of 95 % after 10,000 cycles.[29] Considering slightly smaller values but after cycling to much higher cell voltages provides a positive perspective for the longevity of SiOC-CDC electrodes.

4. Conclusions

In our study we have presented a novel approach to produce ultrafine SiOC electrospun fibers without using any carrier polymer. This new approach, based on the pre-crosslinking of silicone resin, and utilization of a latent catalyst, resulted in the stabilization of the fiber shape prior to heat treatment at high temperatures. After pyrolysis at 1200 °C, non-porous SiOC fibers were obtained.

The material was evaluated as precursor for highly porous SiOC-CDC fibers, leading to partially graphitized carbon with average correlation length of ca. 3 nm and a BET specific surface area of 3089 $m^2 \cdot g^{-1}$. Transitioning from electrospinning to electrospraying, SiOC-CDC beads were produced with a diameter of around 3 μm. The beads, using the same chlorine gas treatment parameters as the fibers, showed a lower specific pore volume related to incomplete CDC transformation.

The synthesized fiber mats were evaluated as binder-free electrode for supercapacitors and compared to the performance of PTFE-bound electrodes composed of crushed fiber mats or beads. The specific capacitance was similar for the fibers with PTFE and for the bead electrodes but higher for the freestanding fiber mat. This is indicating the pore blocking effect by the polymer binder. The binder-free free-standing fiber mat presented a much higher power handling ability, retaining at 100 $A \cdot g^{-1}$ still 63 % of the capacitance at 0.1 $A \cdot g^{-1}$ compared to an almost complete loss of the energy storage ability of binder-containing electrode films at such high rates.

In all cases, the SiOC-beads, present similar electrochemical performance as the fibers, but a lower specific surface area. Obviously, an enhanced porosity does not necessarily translate to an increased capacitance in organic media when using nanoporous carbons with such a high specific surface area. These findings perfectly align with what has been shown by Barbieri et al.[66] The SiOC-CDC present a higher capacitance in organic electrolyte (135 $F \cdot g^{-1}$, **Figure 6a**) compared to other metal carbide-derived carbon fibers synthesize (120 $F \cdot g^{-1}$),[22] and to other metal carbide-derived carbon powders (100-130 $F \cdot g^{-1}$).[29, 67, 68]

Acknowledgments

References

[1] P. Simon, Y. Gogotsi, Nature Materials, 7 (2008) 845-854.
[2] S. Zhang, N. Pan, Advanced Energy Materials, 5 (2015) 1401401.
[3] M. Lu, F. Beguin, E. Frackowiak, Supercapacitors: Materials, Systems and Applications, Wiley-VCH, 2013.
[4] N. Jäckel, D. Weingarth, M. Zeiger, M. Aslan, I. Grobelsek, V. Presser, Journal of Power Sources, 272 (2014) 1122-1133.
[5] M. Aslan, D. Weingarth, N. Jäckel, J.S. Atchison, I. Grobelsek, V. Presser, Journal of Power Sources, 266 (2014) 374-383.
[6] J. Che, P. Chen, M.B. Chan-Park, Journal of Materials Chemistry A, 1 (2013) 4057-4066.

[7] L.T. Le, M.H. Ervin, H. Qiu, B.E. Fuchs, W.Y. Lee, Electrochemistry Communications, 13 (2011) 355-358.

[8] B.-H. Kim, K.S. Yang, H.-G. Woo, K. Oshida, Synthetic Metals, 161 (2011) 1211-1216.

[9] C. Tran, V. Kalra, Journal of Power Sources, 235 (2013) 289-296.

[10] M. Zeiger, D. Weingarth, V. Presser, ChemElectroChem, 2 (2015) 1117-1127.

[11] E. Frackowiak, Physical Chemistry Chemical Physics, 9 (2007) 1774-1785.

[12] V. Presser, M. Heon, Y. Gogotsi, Advanced Functional Materials, 21 (2011) 810-833.

[13] W.A. Mohun, in: Proceedings of the 4th Biennial Conference on Carbon Pergamon, Oxford, 1959, pp. 443-453.

[14] C. Vakifahmetoglu, V. Presser, S.-H. Yeon, P. Colombo, Y. Gogotsi, Microporous and Mesoporous Materials, 144 (2011) 105-112.

[15] L. Borchardt, C. Hoffmann, M. Oschatz, L. Mammitzsch, U. Petasch, M. Herrmann, S. Kaskel, Chemical Society Reviews, 41 (2012) 5053-5067.

[16] J.K. Ewert, D. Weingarth, C. Denner, M. Friedrich, M. Zeiger, A. Schreiber, N. Jackel, V. Presser, R. Kempe, Journal of Materials Chemistry A, (2015) 18906-18912.

[17] L. Borchardt, M. Oschatz, S. Kaskel, Materials Horizons, 1 (2014) 157-168.

[18] W. Gu, G. Yushin, Wiley Interdisciplinary Reviews: Energy and Environment, 3 (2014) 424-473.

[19] S.R. Varanasi, S.K. Bhatia, The Journal of Physical Chemistry C, 119 (2015) 17573-17584.

[20] P. Huang, M. Heon, D. Pech, M. Brunet, P.-L. Taberna, Y. Gogotsi, S. Lofland, J.D. Hettinger, P. Simon, Journal of Power Sources, 225 (2013) 240-244.

[21] M. Oschatz, M. Zeiger, N. Jäckel, P. Strubel, L. Borchardt, R. Reinhold, W. Nickel, J. Eckert, V. Presser, S. Kaskel, Journal of Materials Chemistry A, 3 (2015) 17983-17990.

[22] Y. Gao, V. Presser, L. Zhang, J.J. Niu, J.K. McDonough, C.R. Pérez, H. Lin, H. Fong, Y. Gogotsi, Journal of Power Sources, 201 (2012) 368-375.

[23] M. Rose, E. Kockrick, I. Senkovska, S. Kaskel, Carbon, 48 (2010) 403-407.

[24] C.R. Pérez, S.-H. Yeon, J. Ségalini, V. Presser, P.-L. Taberna, P. Simon, Y. Gogotsi, Advanced Functional Materials, 23 (2013) 1081-1089.

[25] T. Fey, B. Zierath, A.M. Kern, P. Greil, B.J.M. Etzold, Carbon, 70 (2014) 30-37.

[26] R.K. Dash, A. Nikitin, Y. Gogotsi, Microporous and Mesoporous Materials, 72 (2004) 203-208.

[27] A. Jänes, T. Thomberg, E. Lust, Carbon, 45 (2007) 2717-2722.

[28] L.G.B. Camargo, B.G. Palazzo, G. Taylor, Z.A. Norris, Y.K. Patel, J.D. Hettinger, L. Yu, Journal of The Electrochemical Society, 162 (2015) H811-H815.

[29] A. Meier, M. Weinberger, K. Pinkert, M. Oschatz, S. Paasch, L. Giebeler, H. Althues, E. Brunner, J. Eckert, S. Kaskel, Microporous and Mesoporous Materials, 188 (2014) 140-148.

[30] J. Xu, R. Zhang, P. Chen, D. Shen, X. Ye, S. Ge, Carbon, 64 (2013) 444-455.

[31] J.S. Atchison, M. Zeiger, A. Tolosa, L.M. Funke, N. Jackel, V. Presser, RSC Advances, 5 (2015) 35683-35692.

[32] J.R. Martin, L. Borchardt, M. Oschatz, G. Mondin, S. Kaskel, Chemie Ingenieur Technik, 85 (2013) 1742-1748.

[33] F.I. Hurwitz, L. Hyatt, J. Gorecki, L. D´Amore, in: 1 1 th Annual Conference on Composites, Advanced Ceramics, and Composite Materials cosponsored by the American Ceramic Society, DOD, and NASA, Cocoa Beach, Florida, 1987.

[34] D.-S. Ruan, Y.-L. Li, L. Wang, D. Su, F. Hou, Journal of Sol-Gel Science and Technology, 56 (2010) 184-190.

[35] C. Vakifahmetoglu, Advances in Applied Ceramics, 110 (2011) 188-204.

[36] S. Cavaliere, Elecrospinning nanofibers for low-temperature PEMFC in: Electrospinning for Advanced Energy and Environmental Applications, CRC Press. Taylor and francis group, 2015, pp. 37-38.

[37] Y.E. Roginskaya, A.D. Shepelev, T.K. Tenchurin, E.D. Politova, B.A. Loginov, N.V. Kozlova, T.L. Kulova, A.M. Skundin, Russian Journal of Physical Chemistry A, 85 (2011) 2013-2019.

[38] A. Guo, M. Roso, M. Modesti, J. Liu, P. Colombo, Journal of Applied Polymer Science, 131 (2014) 39836.

[39] C.A. Schneider, W.S. Rasband, K.W. Eliceiri, Nat Meth, 9 (2012) 671-675.

[40] S. Brunauer, P.H. Emmett, E. Teller, Journal of the American Chemical Society, 60 (1938) 309-319.

[41] G.Y. Gor, M. Thommes, K.A. Cychosz, A.V. Neimark, Carbon, 50 (2012) 1583-1590.

[42] P.I. Ravikovitch, G.L. Haller, A.V. Neimark, Advances in Colloid and Interface Science, 76–77 (1998) 203-226.

[43] A. Vishnyakov, P.I. Ravikovitch, A.V. Neimark, Langmuir, 15 (1999) 8736-8742.

[44] F. Wolff, C. Kugler, H. Münstedt, Rheologica Acta, 51 (2012) 71-80.

[45] J.D.B. Smith, Journal of Applied Polymer Science, 26 (1981) 979-986.

[46] P.J. Flory, A. Vrij, Journal of the American Chemical Society, 85 (1963) 3548-3553.

[47] A.B. Strong, Fundamentals of Composites Manufacturing, Second Edition: Materials, Methods and Applications, Second edition ed., Society of Manufacturing Engineers, 2008.

[48] S. Koombhongse, W. Liu, D.H. Reneker, Journal of Polymer Science Part B: Polymer Physics, 39 (2001) 2598-2606.

[49] B.P. Whim, P.G. Johnson, Directory of Solvents, Springer Netherlands, 2012.

[50] P. Colombo, G. Mera, R. Riedel, G.D. Sorarù, Journal of the American Ceramic Society, (2010) no-no.

[51] G. Socrates, Infrared and Raman Characteristic Group Frequencies: Tables and Charts, Wiley, 2004.

[52] T. Oh, C. Choi, Journal of the Korean Physical Society, 56(4) (2010) 1150-1155.

[53] A.C. Ferrari, Solid State Communications, 143 (2007) 47-57.

[54] A.C. Ferrari, D.M. Basko, Nat Nano, 8 (2013) 235-246.

[55] G.A. Zickler, B. Smarsly, N. Gierlinger, H. Peterlik, O. Paris, Carbon, 44 (2006) 3239-3246.

[56] F. Tuinstra, J.L. Koenig, The Journal of Chemical Physics, 53 (1970) 1126-1130.

[57] L. Zhang, D. Dai, R. Zhang, Polymers for Advanced Technologies, 8 (1997) 662-665.

[58] K. Faber, F. Badaczewski, M. Oschatz, G. Mondin, W. Nickel, S. Kaskel, B.M. Smarsly, The Journal of Physical Chemistry C, 118 (2014) 15705-15715.

[59] P. Scherrer, Nachrichten von der Gesellschaft der Wissenschaften zu Göttingen, Mathematisch-Physikalische Klasse, (1918) 98-100.

[60] M. Thommes, K. Kaneko, A.V. Neimark, J.P. Olivier, F. Rodriguez-Reinoso, J. Rouquerol, K.S.W. Sing, in: I.D. Gruyter (Ed.), 2015.

[61] P.B. Balbuena, K.E. Gubbins, Langmuir, 9 (1993) 1801-1814.

[62] Y. Korenblit, M. Rose, E. Kockrick, L. Borchardt, A. Kvit, S. Kaskel, G. Yushin, ACS Nano, 4 (2010) 1337-1344.

[63] D. Weingarth, M. Zeiger, N. Jäckel, M. Aslan, G. Feng, V. Presser, Advanced Energy Materials, 4 (2014) 1400316.

[64] J. Chmiola, C. Largeot, P.-L. Taberna, P. Simon, Y. Gogotsi, Angewandte Chemie International Edition, 47 (2008) 3392-3395.

[65] R. Kötz, M. Carlen, Electrochimica Acta, 45 (2000) 2483-2498.

[66] O. Barbieri, M. Hahn, A. Herzog, R. Kötz, Carbon, 43 (2005) 1303-1310.

[67] R. Dash, J. Chmiola, G. Yushin, Y. Gogotsi, G. Laudisio, J. Singer, J. Fischer, S. Kucheyev, Carbon, 44 (2006) 2489-2497.

[68] C. Portet, G. Yushin, Y. Gogotsi, Journal of the Electrochemical Society, 155 (2008) A531-A536.

Tables

Table 1   Melting point and molecular weight (M_w; M_n: number average molecular weight) of as received and pre-crosslinked silicone resins.

Sample	Melting point (°C)	M_w (g·mol^{-1})	M_w/M_n
H44 as-received	42	1084	4.1
H44-22	51	1458	4.3
H44-26	58	1746	4.6

Table 2   Overview of the results of the chemical composition determined by EDX, gas sorption analysis using the BET equation, and Raman peak analysis.

Sample	Composition	BET SSA (m^2·g^{-1})	I_D/I_G-ratio	FWHM D-mode (cm^{-1})	FWHM G-mode (cm^{-1})
SiOC fibers	$SiO_{1.6}C_{0.2}$ + 2.4 C_{free}	11	1.46	169.1±2.1	68.7±0.8
SiOC beads	$SiO_{1.6}C_{0.2}$ + 2.3 C_{free}	10	1.35	141.4±2.3	65.0±0.8
SiOC-CDC fibers	C + 0.02 O	3089	1.63	75.2±0.8	59.5±0.9
SiOC-CDC beads	C + 0.02 O +0.02 Cl	2227	1.78	68.0±0.7	65.8±1.0

Table 3   Equivalent distributed resistance (EDR), equivalent serial resistance (ESR) and the exponent of the constant phase element (CPE) of free-standing fiber electrode and PTFE-bounded electrodes. Values were calculated from Nyquist plots.

Electrode	ESR (Ω·cm^2)	EDR (Ω·cm^2)	CPE exponent
Fibers: free-standing	0.62	0.09	0.83

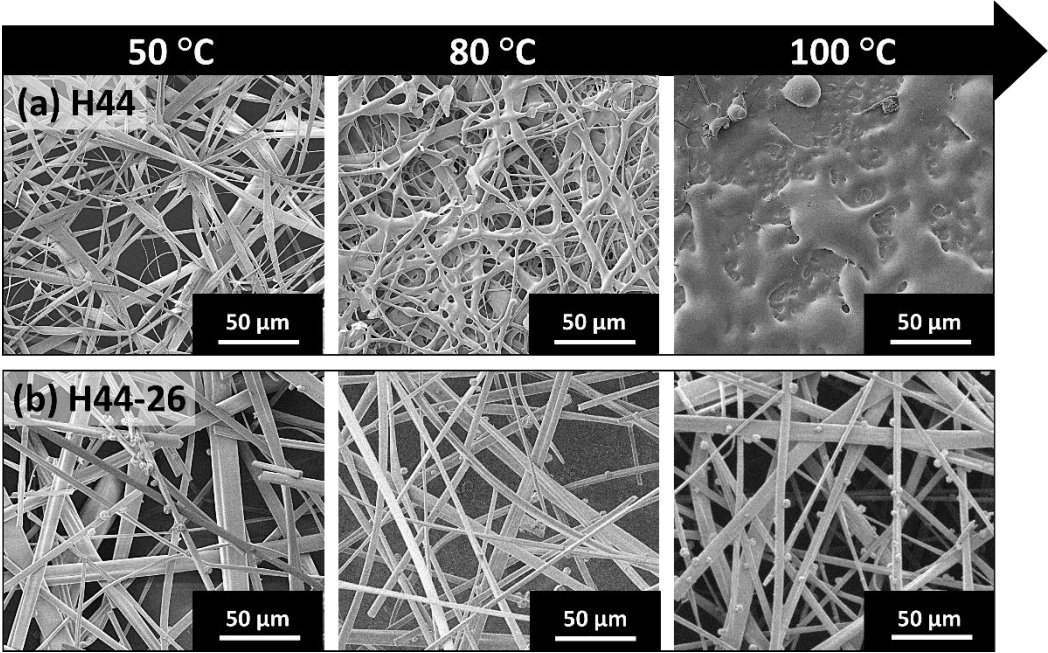|			
Fibers: PTFE-bound	0.82	0.17	0.95
Beads: PTFE-bound	0.81	0.15	0.96

Figures

Fig. 1: SEM images of electrospun mats of H44 (a) and H44-26 (b), treated at different temperatures.
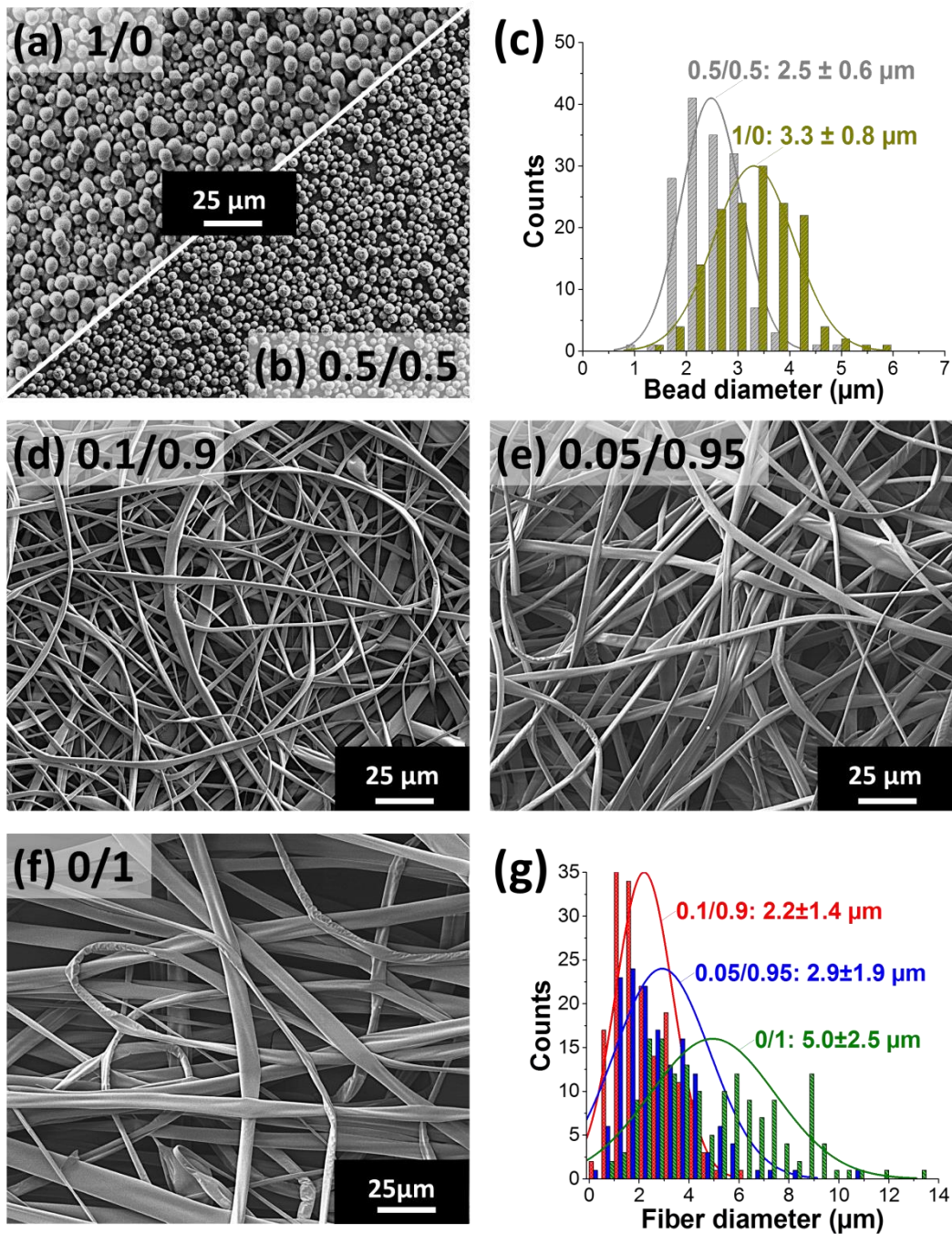
Fig. 2 : SEM micrographs of H44-26 in DMF/EtOH at different mass ratios. Electrosprayed beads formed at ratios 1/0 (a) and 0.5/0.5 (b). Bead diameter distribution (c). Electrospun fibers/ribbons formed at ratios 0.1/0.9 (d), 0.05/0.95 (e) and 0/1 (f). Fiber diameter distribution of as spun fibers (g), the Gaussian lines are inserted to guide the eye.
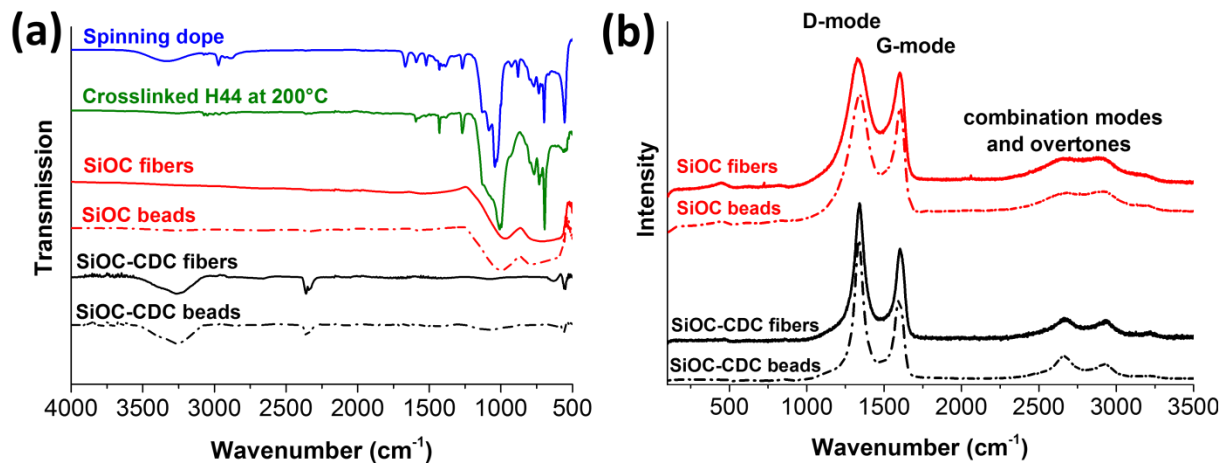
Fig. 3 : Fourier transformed infrared (FTIR) spectra of spinning dope, crosslinked H44, SiOC and SiOC-CDC fibers and beads (a). Raman spectra of SiOC and SiOC-CDC fibers and beads (b).
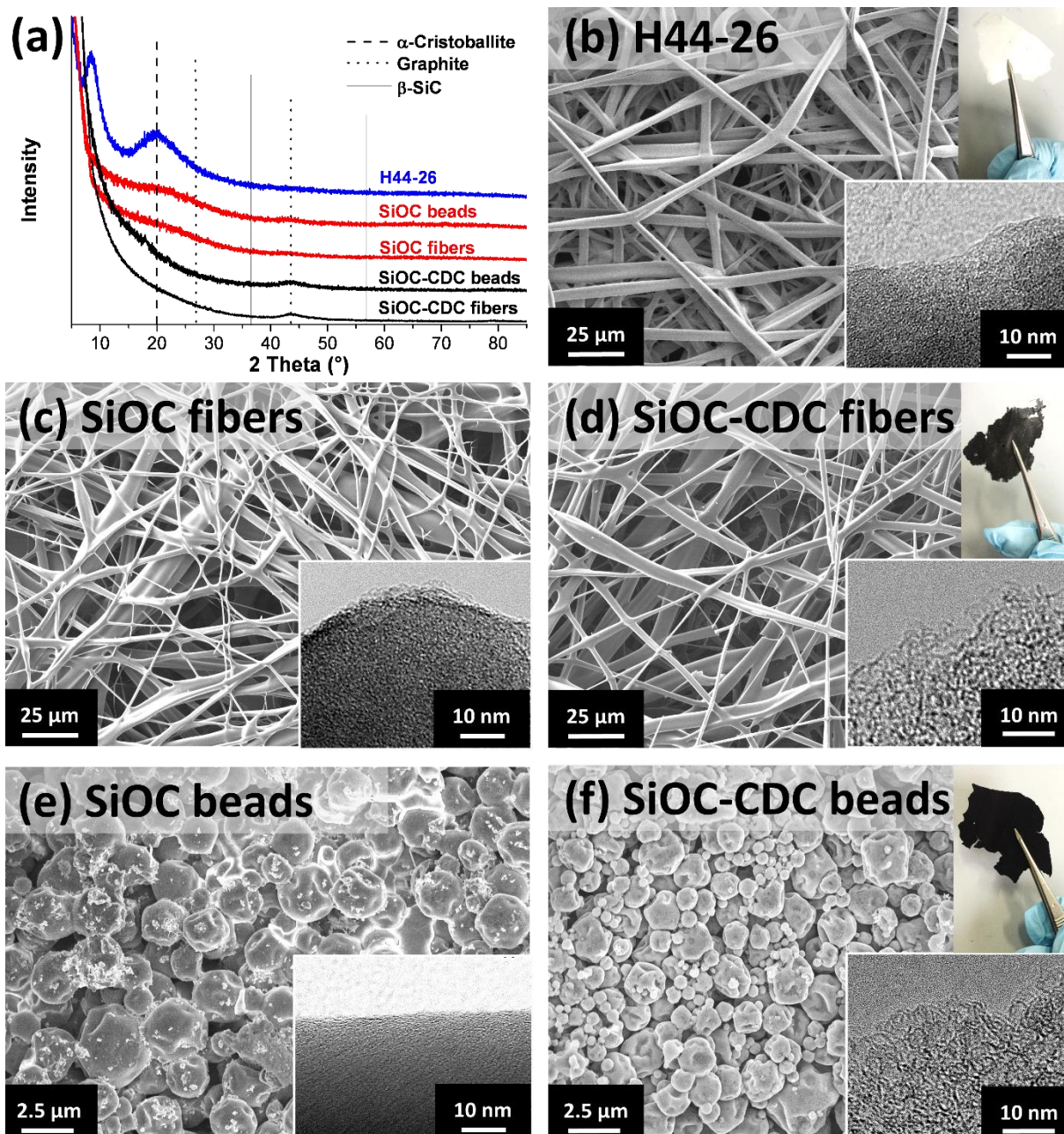
Fig. 4: (a) XRD patterns and SEM and TEM micrographs of polymer H44-26 (b), SiOC (c,e), and SiOC-CDC (d,f). The insets show digital photographs of the free-standing fiber mats before and after pyrolysis, and beads PTFE-bound electrode.
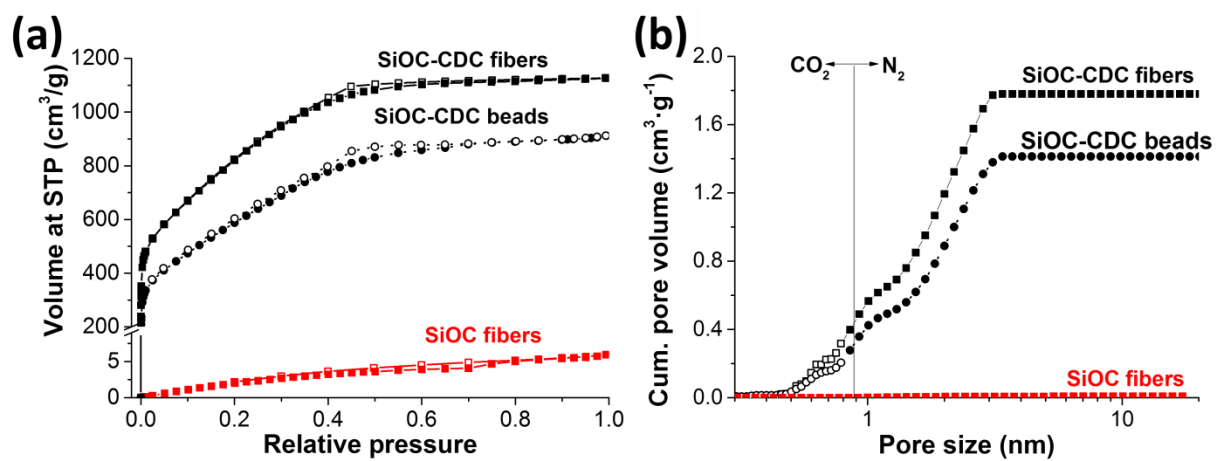
Fig. 5: (a) N_2 gas sorption isotherms for SiOC and SiOC-CDC fiber and beads. (b) Cumulative pore volume distribution using NLDFT and QSDFT models for CO_2 and N_2 adsorption, respectively.
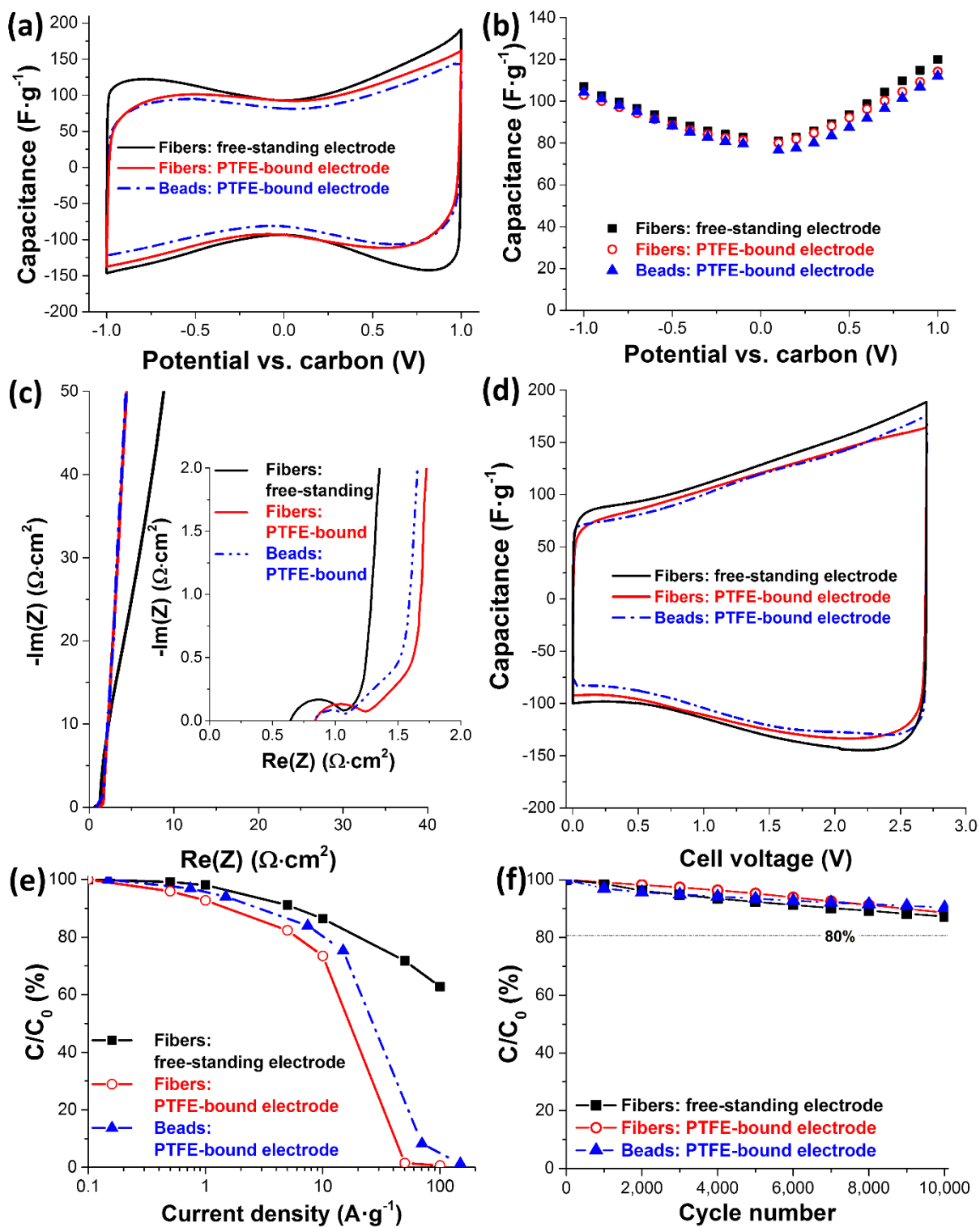
Fig. 6: Electrochemical performance of the free-standing SiOC-CDC fiber mat electrode and PTFE containing electrodes. (a) Cyclic voltammograms at 10 mV·s⁻¹ and (b) specific capacitance by GCPL at 2 A·g⁻¹ with a holding time of 10 min for half-cell configuration. (c) Nyquist plot (inset shows a zoomed range). (d) Cyclic voltammograms at 10 mV·s⁻¹ for a full-cell. (e) Rate handing capability in full-cell by GCPL at 1 V. (f) Electrochemical performance stability surveyed by voltage sweeping up to a cell voltage of 2.7 V. The dashed line represents a capacitive fade of 20 % (failure criterion in industry) and was not crossed by any material.